JOURNAL OF SOLID STATE CHEMISTRY **134,** 219–226 (1997)
ARTICLE NO. SC977483

New Bi–*Ln*–V–O Anionic Conductors with δ-Bi_2O_3 Fluorite-Type Structure (*Ln* = Y, Sm, Eu, Gd, Tb, Dy, Er, Yb)

N. Portefaix, P. Conflant, J. C. Boivin, J. P. Wignacourt, and M. Drache[1]

Laboratoire de Cristallochimie et Physiochimie du Solide, URA CNRS 452, ENSCL et USTL, BP 108, 59652 Villeneuve d'Ascq Cedex, France

Received December 26, 1996; in revised form May 15, 1997; accepted May 22, 1997

An extensive investigation of Bi_2O_3–Ln_2O_3–V_2O_5 systems (*Ln* = Y, Sm, Eu, Gd, Tb, Dy, Er, Yb) yields preservation of the metastable fcc δ-Bi_2O_3 structure in large composition ranges by air-cooling from the high temperature δ equilibrium domain. Partial substitution of V for *Ln* in $Bi_{0.85}Ln_{0.15(1-y)}V_{0.15y}O_{1.5+0.15y}$ samples ($0 \leq y \leq 0.45$) results in a lowering of the equilibrium temperatures, as well as an increase of the stability of the related quenched phases. The best stability is observed for samples corresponding to $y = 0.3$. The anionic conductivity reaches 10^{-3} S/cm at 300°C and 0.5 S/cm at 700°C for $Bi_{0.85}Tb_{0.105}V_{0.045}O_{1.545}$.

INTRODUCTION

The fcc high temperature δ-Bi_2O_3 form, which is only stable between 730 and 825°C, is well known for its attractive anionic conduction properties (1). This behavior is related to the occurrence of a highly disordered oxide ion deficient network (2). Partial substitution for Bi^{3+} by numerous cations can allow the δ structure to be preserved at room temperature (3–14). However, the "stabilization" strongly depends on the cooling conditions of the samples from the equilibrium domain. For example, the δ structure is not observed at room temperature in both Bi_2O_3–CaO and Bi_2O_3–PbO systems when the samples are air-quenched in alumina crucibles (15, 16). However, only for the Bi_2O_3–CaO system, δ is easily preserved when the samples are air-cooled down in gold crucibles.

Investigations in the Bi–Ca–Pb–O system clearly evidence the favorable effect of a double cationic substitution since the δ-Bi_2O_3-type phase is then easily stabilized under soft conditions, i.e., air-quenched samples in alumina crucibles. A comparison between the behavior upon annealing of Bi–Ca–Pb–O and Bi–*Ln*–Pb–O samples shows that the lanthanide δ stabilized phases exhibit a better stability than the calcium derivates. However, the stability enhancement is accompanied by a decrease in the ionic conductivity due to the presence of a lower number of oxygen vacancies. The influence of the nature of the doping cation has also been examined. For both stable and metastable δ phases, the conductivity of fixed bismuth content samples increases with the proportion of Pb^{2+} cations (11, 17). This is mainly due to the higher polarizability of Pb^{2+} than that of Ca^{2+} or Ln^{3+}.

Recent investigations in Bi–V–O and Bi–(V, *M*)–O systems have led to the discovery of a new family of solid electrolyte named BIMEVOX with very high oxide ion conductivity (18, 19). In this family, the cooperative role of the bismuth lone pair and the highly disordered vanadium coordination polyhedra has been emphasized.

The present work deals with the results of investigations of several (Bi–*Ln*)–V–O mixed oxide systems. Particular attention has been focused on the relationship between the composition (i.e., average size of cations, vacancy rate), the stability of the quenched δ fluorite structure, and the ionic conductivity.

EXPERIMENTAL

Powder samples were prepared by solid state reaction between Bi_2O_3 (purity $\geq$ 99.6%), V_2O_5 (purity $\geq$ 99.9%), and Ln_2O_3 (purity $\geq$ 99.99%). To eliminate any traces of carbonates or hydroxides, Bi_2O_3 and rare earth oxides were previously heated for 12 h respectively at 600°C for Bi_2O_3, 300°C for Y and Er oxides, and 700°C for the other rare earth oxides.

The reactants were weighted to prepare the $Bi_{1-x}Ln_{x(1-y)}V_{xy}O_{1.5+xy}$ samples. They were thoroughly ground in an agate mortar and heated at 750°C for 15 h in alumina crucibles. After grinding, the samples were heated in alumina crucibles at 800°C for 15 h and air quenched. The resulting single or mixed phases were analyzed by X-ray diffraction (XRD) using a Guinier de Wolff camera (λCu$K\alpha$). The treatment of each sample was stopped as soon as the X-ray pattern was characteristic of the fcc δ structure. Otherwise, one or several additional thermal treatments

[1] To whom correspondence should be addressed.

0022-4596/97 $25.00

were performed for a few hours, increasing the temperature by 50°C each time. This repetitive process was stopped as soon as the melting temperature of the products was reached.

The refined parameters of room temperature unit cells were obtained from X-ray patterns using NH_4Br as an internal standard. Density measurements were performed using an automated Micromeritics Accupyc 1330 apparatus equipped with a 1 cm^3 cell.

The stability of the quenched phase was evaluated during dynamic heating cycles and after isothermal long-time annealings. Differential thermal analyses (DTA) were performed in gold crucibles, using a Dupont 1600 cell and 1090B analyzer (heating–cooling rates 300°C/h). The final residues were analyzed by XRD. X-ray thermodiffractometry studies were carried out using either a Siemens D5000 X-ray diffractometer equipped with a Siemens HTK10 high temperature device (platinum sample holder; average heating rate, 400°C/h; air gas flow) or a Guinier–Lenné camera (gold grid sample holder; heating rate, 10–20°C/h).

Electrochemical measurements were performed on sintered materials. Cylindrical pellets (diameter 5 mm, thickness ca. 3 mm for conductivity studies, and diameter 13 mm, thickness ca. 3 mm for oxygen transport measurements) were obtained using a conventional press and were sintered for 15 h at 25°C below their melting temperature. After air-quenching, the compactness was at least 80%. In all cases, XRD examination of a similar pellet submitted simultaneously to the same treatment permitted to control the purity of the initially quenched δ phase. The final phases were also identified after experiments.

For conductivity measurements, gold electrodes were vacuum deposited on both flat surfaces of the pellets. The conductivity was determined by impedance spectroscopy in the range 1–10^6 Hz using a Solartron SI 1255 Schlumberger frequency response analyzer: each set of values was recorded at a given temperature after 1 h stabilization.

Oxygen transport numbers versus temperature were determined by measuring the emf of an air–oxygen concentration cell.

RESULTS

A domain of δ structure was stabilized down to room temperature for all the investigated samples. However, as expected, the extent of the quenching domain depends on the nature of the rare earth. As general features:

— The limits vary in the range $0.1 \leq x \leq 0.5$ and $0 \leq y \leq 0.6$.

— The treatment temperature required to reach the δ phase equilibrium domain increases with the rare earth content; e.g., for samples $Bi_{1-x}Eu_xO_{1.5}$ ($y = 0$), the temperature increases from 800°C for $x = 0.1$ to 1050°C for $x = 0.5$.

— For a fixed bismuth concentration, the temperature, which depends on the *Ln* nature, decreases regularly and always reaches a minimum ($y \cong 0.3$ for $x = 0.15$) when vanadium substitutes for *Ln*.

— The extent of the domain decreases as the vanadium oxide proportion increases. Figure 1 presents the largest domain of air quenched δ-Bi_2O_3-type solid solution which

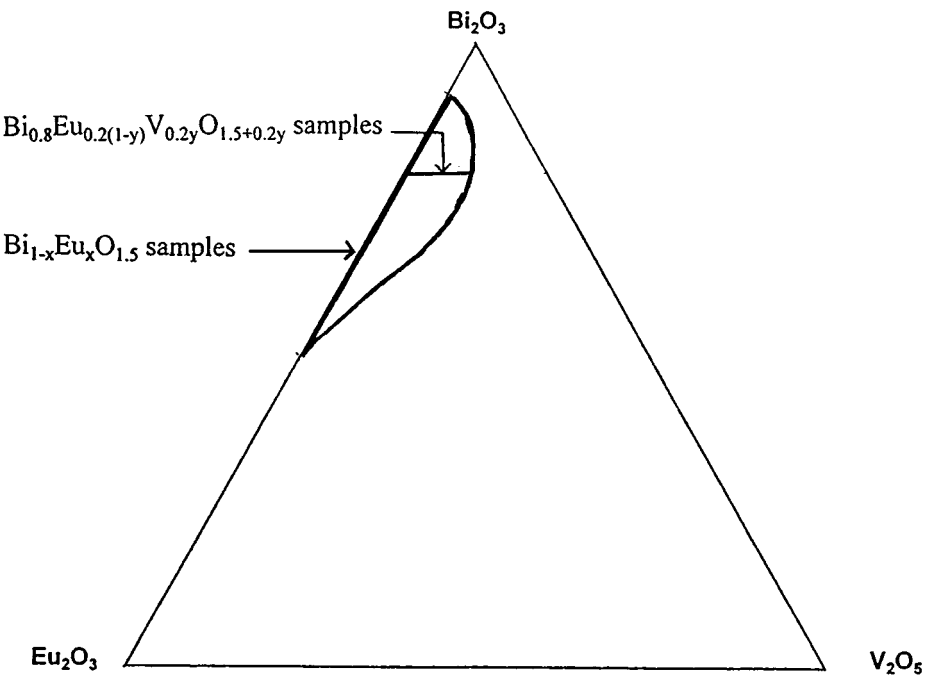

FIG. 1. Air-quenching domain of δ in the Bi_2O_3–Eu_2O_3–V_2O_5 system.

was evidenced for the system Bi_2O_3–Eu_2O_3–V_2O_5. The domain boundary is determined by a number of samples for each given x value (step, 0.05), with a precision generally resulting from the exploration step of $y = 0.15$. Figure 2 shows the corresponding cell parameter evolutions for $Bi_{1-x}Eu_xO_{1.5}$ (a) and $Bi_{0.8}Eu_{0.2(1-y)}V_{0.2y}O_{1.5+0.2y}$ (b). On both lines the variation is in good agreement with Vegard's law.

To analyze the influence of the nature of the rare earth cation and that of the *Ln*/V ratio, systematic comparisons were performed on samples belonging to the same binary line in the different systems. Owing to the correlation systematically observed between the Bi concentration and the ionic conductivity, investigations were performed on samples located in the bismuth rich part of the systems with general formula: $Bi_{0.85}Ln_{0.15(1-y)}V_{0.15y}O_{1.5+0.15y}$.

Density measurements performed for the $Bi_{0.85}Eu_{0.1}V_{0.05}O_{1.55}$ sample confirms that the cubic cell contains four formulas ($d_{exp} = 8.566(2)$, $d_{th} = 8.551$).

Figure 3 shows the evolutions of the cell lattice parameters for *Ln* = Sm, Eu, Gd, Tb, Dy, Y, Er, Yb. It evidences the antagonistic influences of the substitution of Ln^{3+} ($0.86 < r_{VI} < 0.96$) for V^{5+} ($r_{VI} = 0.54$ Å) (20, 21) and the subsequent increase in O^{2-} ions in the unit cell.

— For the largest difference between *Ln* and V cation radii, this effect appears as predominant and the cell parameter decreases as the vanadium concentration increases.

— On the contrary, for smaller rare earth cations, the cell parameter expands according to the increase in the number of O^{2-} ions.

In $Bi_{0.85}Ln_{0.15(1-y)}V_{0.15y}O_{1.5+0.15y}$ samples, a maximum of about 50% of rare earth cations can be substituted by vanadium, while the anionic vacancies rate decreases from 0.25 to 0.2125. This increases the stability of the δ structure: it leads to a decrease in the temperature which is necessary to reach the δ equilibrium domain; a similar phenomenon is observed for the quenched δ phase: DTA plot of a $Bi_{1-x}Ln_xO_{1.5}\delta$ quenched sample ($x \leq 0.3$) shows,

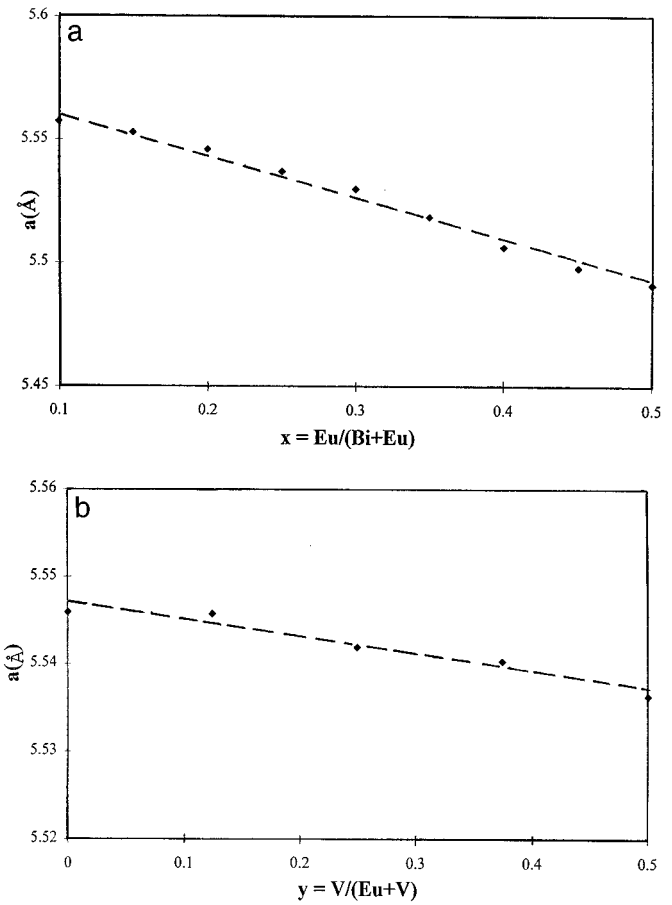

FIG. 2. Cell parameters evolution of quenched δ phase versus the composition for the samples $Bi_{1-x}Eu_xO_{1.5}$ (a) and $Bi_{0.8}Eu_{0.2(1-y)}V_{0.2y}O_{1.5+0.2y}$ (b).

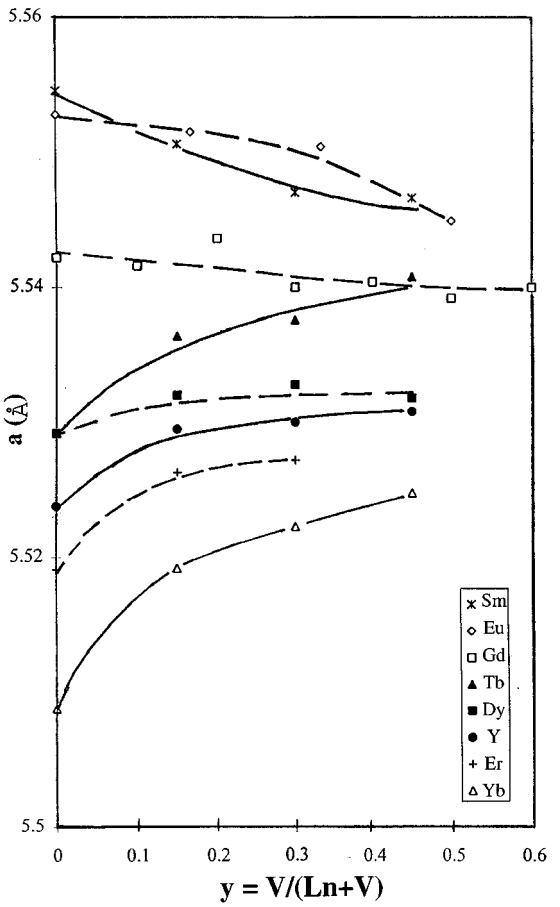

FIG. 3. Cell parameters evolution for $Bi_{0.85}Ln_{0.15(1-y)}V_{0.15y}O_{1.5+0.15y}$ samples.

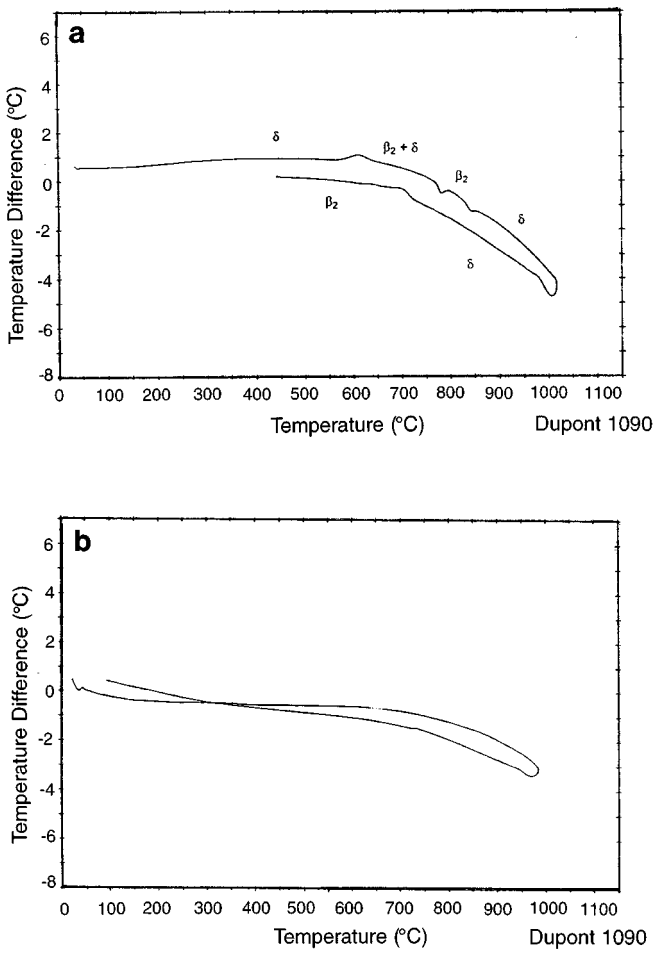

FIG. 4. DTA of air quenched samples $Bi_{0.8}Eu_{0.2}O_{1.5}$ (a) and $Bi_{0.85}Eu_{0.1}V_{0.05}O_{1.55}$ (b).

for the largest rare earth ions (Sm, Eu, Gd), an exothermal transformation in the range 515–635°C (Fig. 4). X-ray analysis evidences that, at this temperature, the δ phase partly converts into a rhombohedral β-type phase (8). The same DTA analysis performed on the $Bi_{0.85}Ln_{0.15(1-y)}V_{0.15y}O_{1.5+0.15y}$ sample ($0.15 \leq y \leq 0.45$) evidences the disappearance of the thermal effect when V replaces *Ln* (Fig. 4b). This result is confirmed by an X-ray pattern which shows the presence of a pure δ phase at the end of the experience.

The influence of the heating rate on the results has been evaluated by dynamic X-ray experiments.

— No transformation of the quenched δ-type phases is evidenced on high temperature X-ray diffraction patterns recorded on a D5000 Siemens diffractometer, between room temperature and 800°C (average heating rate, 400°C/h). Figure 5 shows the lattice parameter evolutions for two different samples $Bi_{0.85}Gd_{0.105}V_{0.045}O_{1.545}$ and $Bi_{0.85}Eu_{0.1}V_{0.05}O_{1.55}$ samples. Both display two almost linear domains with a break around 400°C. No significant modification of the intensity of the X-ray lines can be detected on each side of the transition. This is characteristic of an order–disorder rearrangement which only affects the light atoms (i.e., the oxide ions) of the structure.

— Similar experiments performed using a Guinier–Lenné camera clearly evidenced the influence of the heating rate on the quenched phase behavior. For medium rate ($\cong$ 20°C/h), the pattern only exhibits the cubic lattice parameter thermal expansion (Fig. 6 for a $Bi_{0.85}Eu_{0.10}V_{0.05}O_{1.55}$ sample). For lower values ($\cong$ 10°C/h), an intermediate modification of the quenched phase pattern is observed, for instance between 575 and 675°C for a $Bi_{0.85}Gd_{0.105}V_{0.045}O_{1.545}$ sample.

Furthermore, 24 h annealing at 450°C of quenched δ samples (*Ln* = Eu) without vanadium ($y = 0$) leads to their decomposition into a β rhombohedral phase, whereas the decomposition only occurs near 575°C on DTA curves. Similar annealing of the samples with $y = 0.3$ shows that the decomposition only occurs when the annealing temperature reaches about 650°C. In that case, the δ phase converts into a bcc sillenite-type phase. All these results confirm that the presence of vanadium significantly increases the stability of the fluorite structure.

The conductivity of $Bi_{0.85}Ln_{0.15(1-y)}V_{0.15y}O_{1.5+0.15y}$ phases were measured every 20°C between 300 and 800°C. Samples belonging to the range $0 \leq y \leq 0.45$ were studied for all rare earths. As usual, the pellets being air-quenched after sintering, the electrical measurements performed during the first heating run are not representative of the sample behavior. Thus, Arrhenius plots of the first cooling and second heating process were drawn and interpreted. Figure 7 presents, as examples for *Ln* = Gd, three plots corresponding to the first cooling run. The vanadium-free sample shows two linear evolutions, separated by an intermediate fast changing conductivity zone. These linear parts are both typical of either the δ-Bi_2O_3-type phase (high temperature zone) or the equilibrium phases at low temperature (Fig. 7a). When the vanadium proportion increases ($0 < y < 0.3$), a progressive disappearance of the intermediate zone occurs for most samples. For $y = 0.3$ (Fig. 7b), the fcc δ phase is systematically obtained at the end of the full heating cooling process. For $y = 0.4$–0.5 (Fig. 7c), the fcc phase is partly decomposed at the end of the experiment, although the shape of the Arrhenius plot is similar to the $y = 0.3$ corresponding sample.

A comparison of the conductivities of the $Bi_{0.85}Ln_{0.105}V_{0.045}O_{1.545}$ phases ($x = 0.3$) has been realized. As examples, $\log \sigma = f(1/T)$ is plotted in Fig. 8 for two materials. $Bi_{0.85}Sm_{0.105}V_{0.045}O_{1.545}$ (Fig. 8a) is typical of most investigated samples (*Ln* = Y, Sm–Er). Heating and cooling plots are nearly identical and can be characterized by two apparently linear domains corresponding to the high and low temperature δ forms. For $Bi_{0.85}Yb_{0.105}V_{0.045}O_{1.545}$ (Fig. 8b), the plots appear different in the temperature range

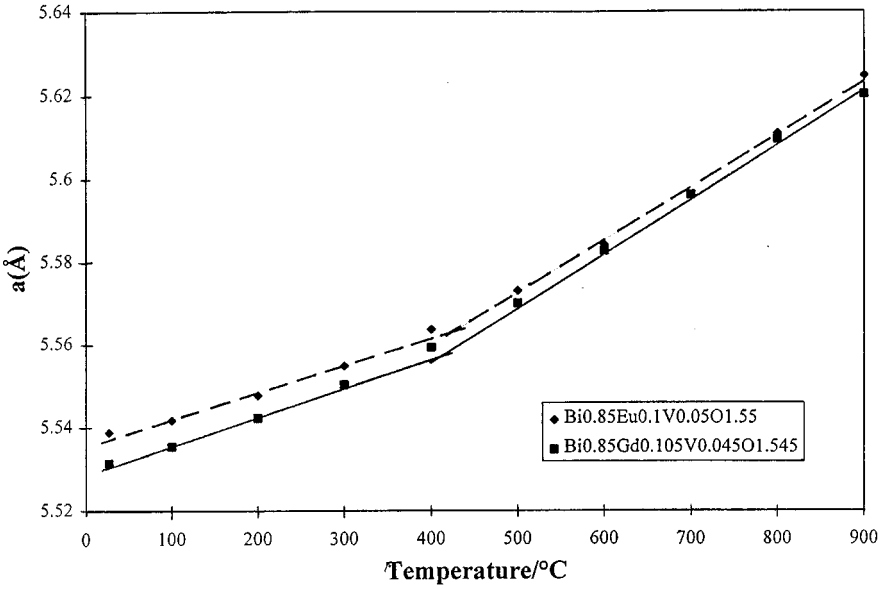

FIG. 5. Cell parameters evolution versus the temperature for samples $Bi_{0.85}Eu_{0.1}V_{0.05}O_{1.55}$ (a) and $Bi_{0.85}Gd_{0.105}V_{0.045}O_{1.545}$ (b).

400–730°C ($\sigma_{heating} < \sigma_{cooling}$). This intermediate zone characterizes a partial decomposition of the low temperature form. On cooling, as it is frequently encountered with mixed bismuth oxides (11), a strong hysteresis occurs and no trace of decomposition of the high temperature form can be detected on the conductivity curve.

Figure 9 shows the evolutions of the apparent activation energies (Fig. 9a) and isothermal conductivities (Fig. 9b) versus the ionic radius of *Ln* ions, measured respectively at 727 and 394°C on the cooling curves. At these temperatures, both phases exhibit an X-ray diffraction pattern characteristic of a δ-type structure. In the high temperature range particularly, the yttrium substituted δ phase is distinguished from the other samples by a high activation energy associated to a low conductivity. This characteristic can be attributed to the low polarizability of Y^{3+} ion due to its Kr-like electronic configuration. In contrast, a minimum of activation energy occurs in the lanthanide series for ions with an electronic configuration close to a half filling of the $4f$ shell. The number of $4f$

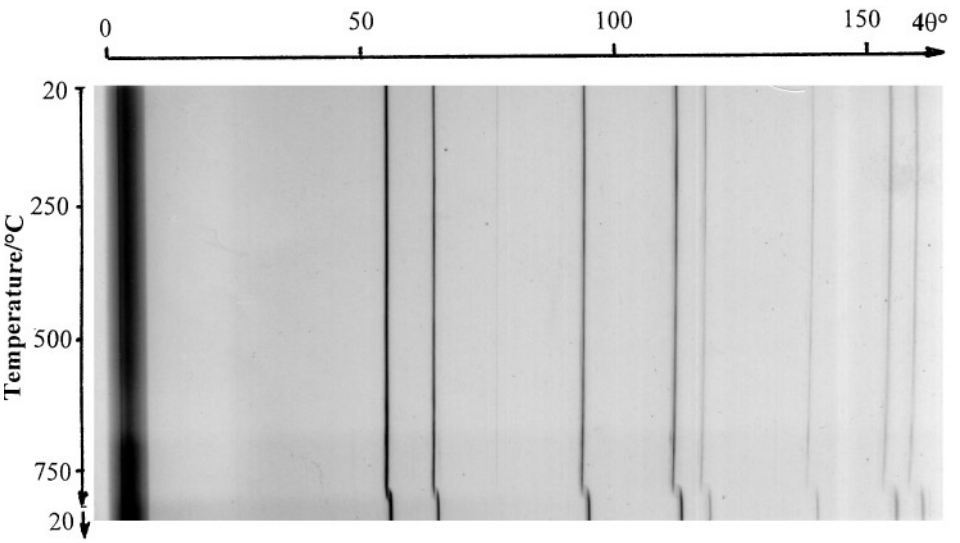

FIG. 6. Guinier–Lenné XRD pattern of $Bi_{0.85}Eu_{0.5}V_{0.01}O_{1.55}$.

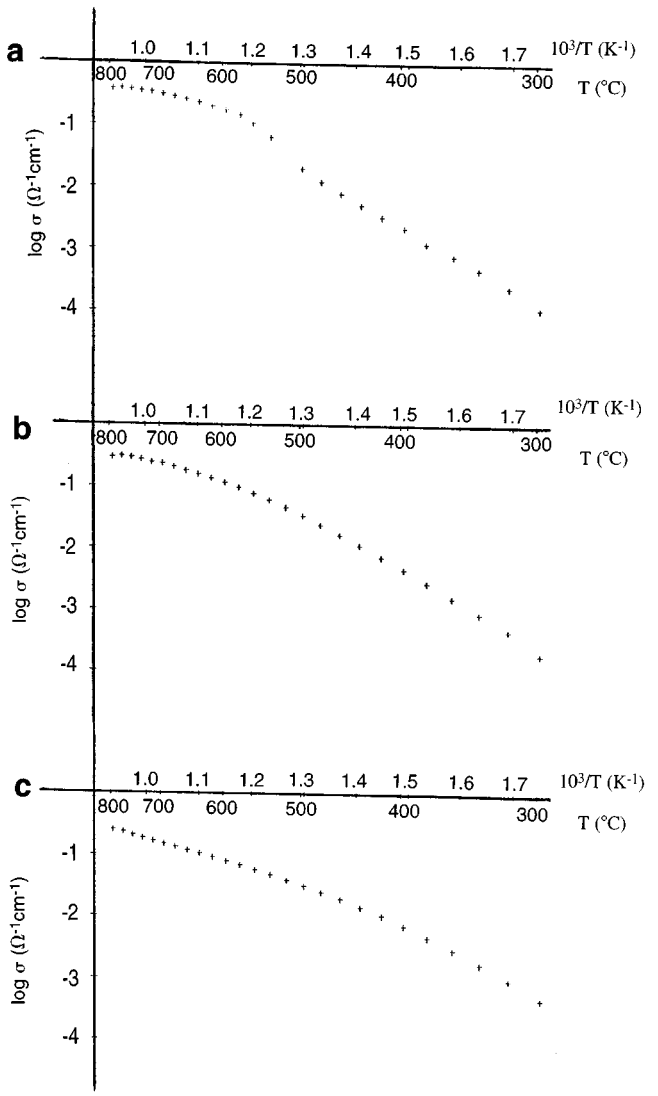

FIG. 7. Arrhenius plots of $Bi_{0.85}Gd_{0.15(1-y)}V_{0.15y}O_{1.5+xy}$ ((a) $y = 0$, (b) $y = 0.3$, (c) $y = 0.5$) during the cooling process.

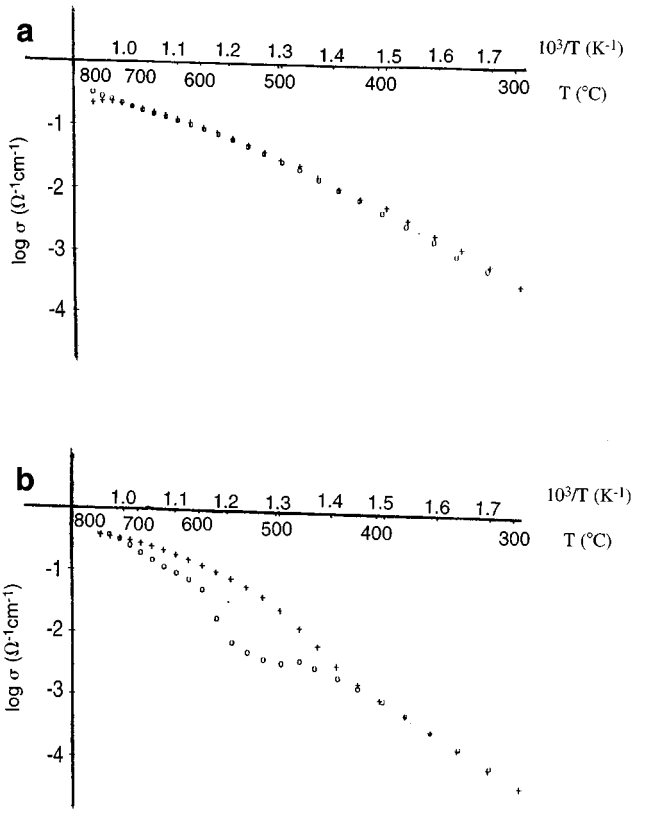

FIG. 8. Arrhenius plots of $Bi_{0.85}Ln_{0.105}V_{0.045}O_{1.545}$ samples (Ln = Sm (a), Yb (b)) during a heating and cooling process.

paired electrons increases from Tb to Yb containing samples; this leads to a decrease in the corresponding cationic polarizability and therefore to the observed increase of the activation energy. Figure 10, which represents the variation of the unit cell parameter as a function of the rare earth cation radius, shows that it is nearly linear and cannot be responsible for the specific evolution reported above.

Figure 11 shows the variances of O^{2-} transport number measured by the emf method, during the first cooling and second heating cycle for $Bi_{0.85}Tb_{0.105}V_{0.045}O_{1.545}$.

Between 250 and 500°C, the measurements are a bit questionable; the lower the temperature, the longer the time necessary to reach an equilibrium value. It is however difficult to know if the transport number values, which always strongly deviate from 1, are significant or must be affected by an unefficient electrode activity upon the oxygen dissociation. However, it would be surprising if electrode efficiency should be the limiting parameter, causing the $E_{meas.}/E_{th.}$ ratio ($E_{th.}$, theoretical potential value from Nernst law, considering that 100% conductivity is from O^{2-} ions) to exhibit a break at the same temperature as that observed for the cubic cell parameter.

For temperature higher than 500°C, in contrast, the equilibrium is reached very quickly. Between 500 and 800°C, the t_O^{2-} transport number varies slightly between 0.95 and 1, proving the predominant anionic character of the conductivity in this whole domain for the δ stabilized phase.

In each case, there is a noticeable difference between heating and cooling plots, with higher transport number values during cooling, just as described before for the conductivity values. This behavior probably has the same origin.

CONCLUSION

These investigations performed in Bi–*Ln*–V–O systems (*Ln* = Y, Sm, Eu, Gd, Tb, Dy, Er, Yb) have evidenced the possibility to preserve easily the cubic δ-Bi_2O_3 structure in

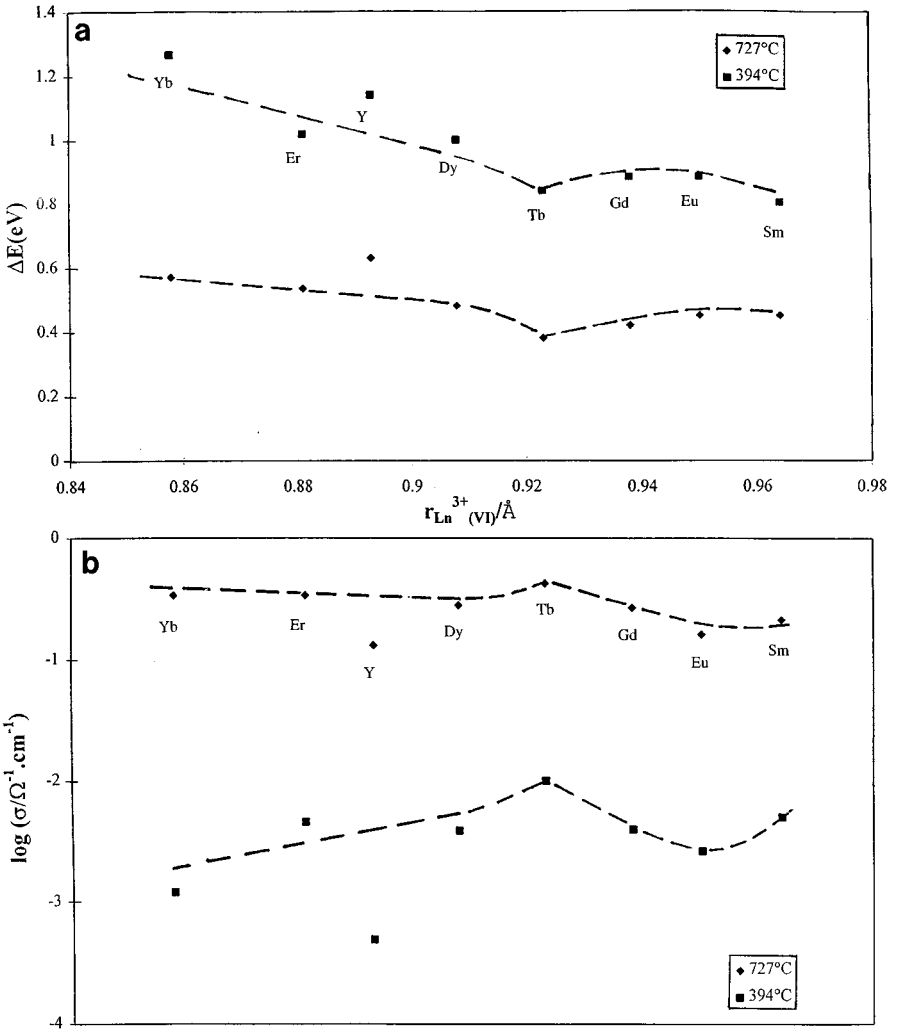

FIG. 9. Evolution of activation energy (a) and isothermal conductivity (b) of high and low temperature phases (727°C, 394°C) of $Bi_{0.85}Ln_{0.105}V_{0.045}O_{1.545}$ versus Ln^{3+} radius.

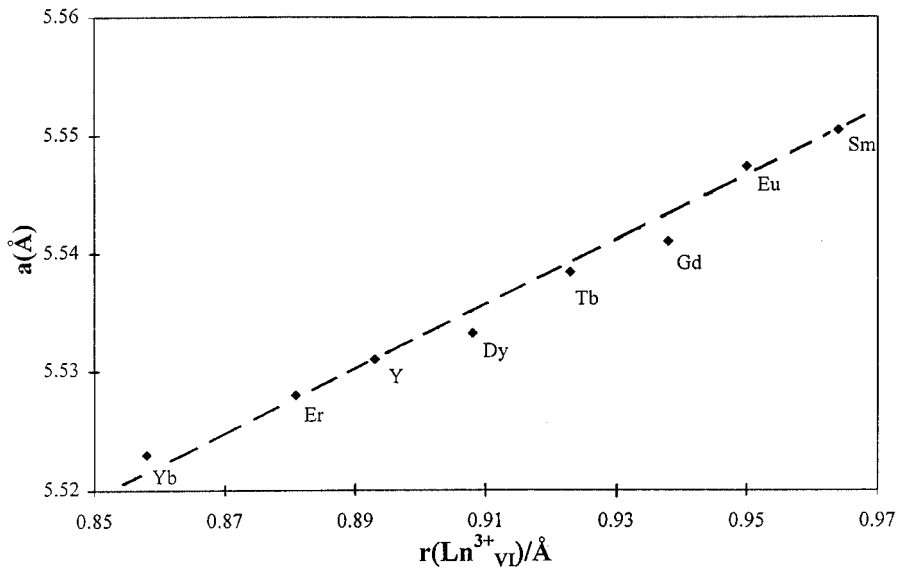

FIG. 10. Cell parameter evolution of $Bi_{0.85}Tb_{0.105}V_{0.045}O_{1.545}$ versus Ln^{3+} radius.

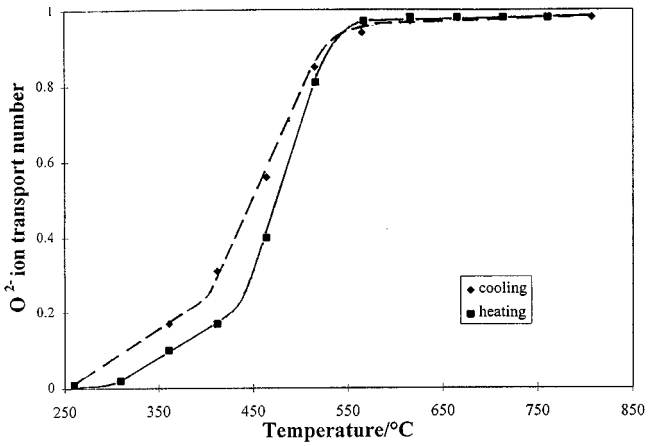

FIG. 11. O^{2-} ion transport number evolution of $Bi_{0.85}Tb_{0.105}V_{0.045}O_{1.545}$ versus temperature during a heating and cooling process.

wide composition ranges, by air quenching from the high temperature equilibrium domain.

The thermal behavior analysis of quenched $Bi_{0.85}Ln_{0.15(1-y)}V_{0.15y}O_{1.5+0.15y}$ samples showed that the stabilized δ phase is always metastable. However, the partial substitution of V for *Ln* decreases the temperature of the equilibrium domain and increases the stability of the corresponding quenched phase. Heating or cooling experiments performed on various samples for rates $\geq 20°C/h$ do not display any trace of decomposition of the δ phase.

The conductivity of $Bi_{0.85}Ln_{0.105}V_{0.045}O_{1.545}$ samples are interesting. For instance, the conductivity of a terbium phase $Bi_{0.85}Tb_{0.105}V_{0.045}O_{1.545}$ is 10^{-3} S/cm at 300°C and 0.5 S/cm at 700°C. As a comparison, at corresponding temperatures, the conductivity is about 0.5×10^{-4} S/cm and 0.3 S/cm for $Bi_{0.8}Er_{0.2}O_{1.5}$ which has been up to now the best reference for the δ-Bi_2O_3 related oxides conductors (22); also in the same temperature range, a BICUVOX sample with composition $Bi_2V_{0.9}Cu_{0.1}O_{5.35}$, which is one of the best oxide conductors evidenced up to now, displays conductivity values varying from 3×10^{-3} to 0.1 S/cm. Additional investigations are now in progress to check the ability of such samples to support high current densities, particularly at low temperature ($t < 500°C$).

REFERENCES

1. T. Takahashi, H. Iwahara, and Y. Nagai, *J. Appl. Electrochem.* **2,** 97 (1972).
2. H. A. Harwig, *Z. Anorg. Allg. Chem.* **444,** 151 (1978).
3. T. Takahashi, H. Iwahara, and T. Arao, *J. Appl. Electrochem.* **5,** 187 (1975).
4. T. Takahashi, T. Esaka, and H. Iwahara, *J. Appl. Electrochem.* **5,** 197 (1975).
5. H. Iwahara, T. Esaka, T. Sato, and T. Takahashi, *J. Solid State Chem.* **39,** 173 (1981).
6. M. J. Verkerk and A. J. Burggraaf, *Solid State Ionics* **3/4,** 463 (1981).
7. A. Watanabe and T. Kikuchi, *Solid State Ionics* **21,** 287 (1986).
8. P. Conflant, C. Follet-Houttemane, and M. Drache, *J. Mater. Chem.* **1**(4), 649 (1991).
9. T. Takahashi and H. Iwahara, *J. Appl. Electrochem.* **3,** 65 (1973).
10. A. El Harrak, P. Conflant, M. Drache, and J. C. Boivin, *J. Chim. Phys.* **88,** 2281 (1991).
11. M. Omari, M. Drache, P. Conflant, and J. C. Boivin, *Solid State Ionics* **40/41,** 929 (1990).
12. G. Meng, C. Chen, X. Han, P. Yang, and D. Peng, *Solid State Ionics* **28/30,** 533 (1988).
13. D. Mercurio, M. El Farissi, B. Frit, J. M. Reau, and J. Senegas, *Solid State Ionics* **39,** 297 (1990).
14. J. Berezovsky, K. H. Liu, and S. X. Dou, *Solid State Ionics* **66,** 201 (1993).
15. P. Conflant, J. C. Boivin, and D. Thomas, *J. Solid State Chem.* **18,** 133 (1976).
16. J. C. Boivin and G. Tridot, *C.R. Acad. Sci.* (*Paris*) *C* **278,** 864 (1974).
17. F. Abraham, J. C. Boivin, G. Mairesse, and G. Nowogrocki, *Solid State Ionics* **40/41,** 934 (1990).
18. M. Drache, P. Conflant, and J. C. Boivin, *Solid State Ionics*, **57,** 245 (1992).
19. E. Pernot, M. Anne, J. Fouletier, R. N. Vannier, and G. Mairesse, *Solid State Ionics* **70/71,** 259 (1994).
20. R. D. Shannon, *Acta Crystallogr. A* **32,** 751 (1976).
21. R. D. Shannon and C. T. Prewitt, *Acta Crystallogr. B* **26,** 1046 (1970).
22. M. J. Verkerk, K. Keizer, and A. J. Burggraaf, *J. Appl. Electrochem.* **10,** 81 (1981).